Hydrol. Earth Syst. Sci. Discuss., doi:10.5194/hess-2017-288, 2017
Manuscript under review for journal Hydrol. Earth Syst. Sci.
Discussion started: 30 May 2017

Hydrology and Earth System Sciences
Discussions
Open Access

CALIBRATING ELECTROMAGNETIC INDUCTION CONDUCTIVITIES WITH TIME-DOMAIN REFLECTOMETRY MEASUREMENTS

Dragonetti[1] Giovanna, Alessandro Comegna[2], Ali Ajeel[2], Gian Piero Deidda[3], Nicola Lamaddalena[1], Giuseppe Rodriguez[4], Giulio Vignoli[3,5], Antonio Coppola[2]*

(1) Mediterranean Agronomic Institute (MAIB) - Land & Water Department, Valenzano (Bari), Italy
(2) University of Basilicata, School of Agricultural, Forestry and Environmental Sciences - Hydraulics and Hydrology Division, Potenza, Italy. e-mail: antonio.coppola@unibas.it
(3) Dipartimento di Ingegneria Civile, Ambientale e Architettura, Università di Cagliari, Cagliari, Italy
(4) Dipartimento di Matematica e Informatica, Università di Cagliari, Cagliari, Italy
(5) Groundwater and Quaternary Geology Mapping Department, Geological Survey of Denmark and Greenland, Aarhus, Denmark

Abstract

This paper deals with the issue of monitoring the horizontal and vertical distribution of bulk electrical conductivity, σ_b, in the soil root zone by using Electromagnetic Induction (EMI) sensors under different water and salinity conditions. In order to deduce the actual distribution of depth-specific σ_b from EMI depth-weighted apparent electrical conductivity (EC_a) measurements, we inverted the signal by using a regularized 1D inversion procedure designed to manage nonlinear multiple EMI-depth responses. The inversion technique is based on the coupling of the damped Gauss-Newton method with truncated generalized singular value decomposition (TGSVD). The ill-posedness of the EMI data inversion is addressed by using a sharp stabilizer term in the objective function. This specific stabilizer promotes the reconstruction of blocky targets, thereby contributing to enhance the spatial resolution of the EMI reconstruction. Time-Domain Reflectometry (TDR) data are used as ground-truth data for calibration of the inversion results. An experimental field was divided into four transects 30 m long and 2.8 m wide, cultivated with green bean and irrigated with water at two different salinity levels and using two different irrigation volumes, to induce different salinity and water contents within the soil profile. For each transect, 26 regularly spaced monitoring sites (1 m apart) were selected for soil measurements using a Geonics EM-38 and a Tektronix Reflectometer. Despite the original discrepancies in the EMI and TDR data, we found a significantly high correlation of the means and standard deviations of the two data series, especially after filtering the TDR data. Based on these findings, the paper introduces a novel methodology to calibrate EMI-based electrical conductivity via TDR direct measurements by simply using the statistics of the two data series.

Introduction

Soil water content and salinity vary in space both vertically and horizontally. Their distribution depends on management practices and on the complex nonlinear processes of soil water flow and solute transport, resulting in variable storages of solutes and water (Coppola et al. 2015).

Monitoring the actual distribution of water and salts in the soil profile explored by roots is crucial to managing irrigation with saline water, while still maintaining an acceptable crop yield. For monitoring water and salts over large areas, there are now non-invasive techniques based on electromagnetic sensors which allow the bulk electrical conductivity of soils, σ_b, to be determined (Sheets and Hendrickx 1995, Corwin and Lesch 2005, Robinson et al. 2012, Doolittle and Brevik 2014, von Hebel et al. 2014) among many others). σ_b depends on soil water content, θ, electrical conductivity of the soil solution (salinity), σ_w, tortuosity of the soil-pore system, τ, and other factors related to the solid phase such as bulk density, clay content and mineralogy.

Electromagnetic induction (EMI) sensors provide measurements of depth-weighted apparent electrical conductivity, EC_a, according to the specific depth distribution of the soil bulk electrical conductivity, σ_b, as well as the depth response function of the sensor used (McNeill 1980). Thus dependence on σ_b makes EC_a sensitive to soil salinity and water content. In principle, specific procedures for estimating salinity and water content may be developed through controlled laboratory experiments where σ_b, σ_w and θ are measured simultaneously (Rhoades and Corwin 1981). That said, to monitor salinity and water content, it is crucial to correctly infer the depth-distribution of σ_b from profile-integrated EC_a readings.

To date, this issue has been tackled by applying two different strategies: The first is to use empirical calibration relations relating the depth-integrated EC_a readings to the σ_b values measured by alternative methods - like Time-Domain Reflectometry (TDR) -within discrete depth intervals (Rhoades and Corwin 1981, Lesch et al. 1992, Triantafilis, Laslett, and McBratney 2000, Amezketa 2006, Yao and Yang 2010, Coppola et al. 2016); The second consists in the 1D inversion of the observations from the EMI sensor to reconstruct the vertical conductivity profile (Borchers, Uram, and Hendrickx 1997, Hendrickx et al. 2002, Santos et al. 2010, Lavoué et al. 2010, Mester et al. 2011, Minsley et al. 2012, Deidda, Fenu, and Rodriguez 2014, von Hebel et al. 2014).

With regard to EC_a inversion, a forward model still commonly used is the cumulative response model or local-sensitivity model (LSM) (McNeill 1980). McNeill's linear approach is well suited to the cases characterized by an induction number, β (defined as the ratio between the coil distance and the skin depth), much smaller than 1. However, because of increasing computing power, improved forward modeling algorithms based on more accurate nonlinear approaches are becoming increasingly common (Hendrickx et al. 2002, Deidda, Fenu, and Rodriguez 2014, Deidda, Bonomi, and Manzi 2003, Lavoué et al. 2010, Santos et al. 2010). For example, these more sophisticated forward modeling codes can cope with a wider range of conductivities for which the assumption β<<1 is not necessarily met.

To obtain reliable vertical distributions of electrical conductivity, the EC_a data used for the inversion should consist of multi-configuration data. Hence, data collection should be performed either with the simultaneous use of different sensors or with different acquisition configurations with only one sensor (different configurations may consist, e.g., in different coil orientations, varying intercoil separations and/or frequencies – see, for example Díaz de Alba and Rodriguez (2016)). Multi-configuration data can be effectively used to invert for vertical electrical conductivity profiling since the EC_a measures actually investigate different, overlapping soil volumes. Devices specifically designed for the simultaneous acquisition of multi-configuration data are currently available. Some of them consist of one transmitter and several receivers with different coil separations and orientations (Santos et al. 2010). If, instead, a sensor with a single intercoil distance is available, a valid alternative to having multi-configuration measurements could be to record the data at different heights above the ground. Unfortunately, like every other physical measurement, frequency-domain electromagnetic measurements are sensitive to noise that is very hard to model effectively. Therefore, for example, as discussed in Lavoué et al. (2010), Mester et al. (2011), and von Hebel et al. (2014), an instrumental shift in conductivity values could be observed due to system miscalibration and the influence of surrounding conditions such as temperature, solar radiation, power supply conditions, the presence of the operator, zero-leveling procedures, cables close to the system and/or the field setup (see, amongst others, (Sudduth, Drummond, and Kitchen 2001, Robinson et al. 2004, Abdu, Robinson, and Jones 2007, Gebbers et al. 2009, Nüsch et al. 2010). Therefore the EC_a data from EMI measurements would generally need proper calibration. One option could be to use soil cores as ground-truth data. In this case, EC_a measurements at the sampling locations are compared against EC_a data predicted by the theoretical forward response applied to the true electrical conductivity distribution measured directly on the soil cores (Triantafilis, Laslett, and McBratney 2000, Moghadas et al. 2012). Clearly, this strategy is extremely time- (and resource-) consuming. To avoid drilling, Lavoué et al. (2010) introduced a calibration method, later also adopted by Mester et al. (2011) and von Hebel et al. (2014), using the electrical conductivity distribution obtained from Electrical Resistivity Tomography (ERT) data as input for electromagnetic forward modeling. The EC_a values predicted on the basis of ERT data were used to remove the observed instrumental shift and correct the measured conductivity values by linear regression. However, a prerequisite for such an approach concerns the reliability of the inversion of the ERT result. This is not only due to the quality of the original data, but also the adopted inversion procedure. Indeed, ERT inversion is an ill-posed problem: its solutions are characterized by non-uniqueness and instability with respect to the input data (Yu and Dougherty 2000, Zhdanov 2002, Günther 2011). In the Tikhonov regularization framework, ill-posedness is addressed by including the available prior information. Such information can be very general. For example, it can be geometrical (i.e., associated to the presence of smooth or sharp boundaries between different lithologies). Clearly, the final result largely reflects the initial guess formalized via the chosen regularization term (Pagliara and Vignoli 2006, Günther 2011, Vignoli, Deiana, and Cassiani 2012, Fiandaca et al. 2015).

When relatively shallow depths have to be explored (1-2m), direct soil sampling and ERT can be effectively replaced by TDR observations. In this line of reasoning, this paper focuses on the use of TDR data to calibrate EC_a measurements obtained via EMI. To do this, a dataset collected during an experiment carried out along four transects under different salinity and water content conditions (and monitored by both EMI and TDR sensors) will be utilized. We first tackle the problem of inferring the soil electrical conductivity distribution from multi-height EC_a

readings via the proper inversion strategy. Then we assess the quality of these reconstructions by using TDR data as ground-truth. In this respect, in the following, we discuss how to effectively compare the σ_b values generated by the EMI inversion with the associated TDR values. In fact, as discussed by (Coppola et al. 2016), because of their relatively smaller observation volume, TDR data provide quasi-pointlike measurements and do not integrate the small-scale variability (of soil water content, solute concentrations, etc.) induced by natural soil heterogeneity. By contrast, EMI data necessarily overrule the small-scale heterogeneities seen by TDR probes as they investigate a much larger volume. Accordingly, the paper provides a methodology to calibrate EMI results by TDR readings. This procedure lies in conditioning the original TDR data and in the statistical characteristics of the two EMI and TDR data series. On the basis of the proposed analysis we discuss the physical reasons for the differences between EMI and TDR-based bulk electrical conductivity and identify a method to effectively transfer the reliable TDR information across the larger volume investigated by EMI.

Materials and Methods

The experiment was carried out at the Mediterranean Agronomic Institute of Bari (MAIB) in south-eastern Italy. The soil was pedologically classified as Colluvic Regosol, consisting of a silty-loam layer of an average depth of 0.6 m on fractured calcarenite bedrock. The experimental set-up (Figure 1) consisted of four transects of 30 m length and 2.8 m width, equipped with a drip irrigation system with five dripper lines at 0.35 m distance and a distance among drippers along each line of 0.2 m, with a dripper discharge of 2 l/h. Green beans were grown in each transect. The irrigation volumes were calculated according to the time-dynamics of water content in the first 0.25 m measured by a TDR probe inserted vertically at the soil surface. TDR readings were taken: i) just before and ii) two hours after every irrigation. Based on the difference between the water content at field capacity and that measured just before irrigation the volumes to bring the soil water content back to the field capacity were able to be calculated.

The four transects were irrigated with water at two different salinity levels and with two different water volumes. Transect 1: 100% of the irrigation water at 1 dSm^{-1} (hereafter 100-1dS); Transect 2: 50% of irrigation water at 1 dSm^{-1} (50-1dS); Transect 3: 100% of the irrigation water at 6 dSm^{-1} (100-6dS); Transect 4: 50% of irrigation water at 6 dSm^{-1} (50-6dS). Water salinity was induced by adding calcium chloride ($CaCl_2$) to tap water. Irrigation volumes were applied every two days.

EMI readings in both horizontal (EC_aH) and vertical magnetic dipoles (EC_aV) configurations were collected by using a Geonics EM38 device (Geonics Limited, Ontario, Canada). The EM38 operates at a frequency of 14.6 kHz with a coil spacing of 1 m, and with an effective measurement depth of ≈0.75 m and ≈1.5 m, respectively, in the horizontal and vertical dipole configurations (McNeill, 1980). The lateral footprint of the EM38 measurement can be considered approximately equal to the vertical one. Thus, the σ_b seen by the EMI in a given discrete depth-layer differs from that seen by a TDR probe in the same depth-layer, due to the very different spatial resolutions.

Hydrol. Earth Syst. Sci. Discuss., doi:10.5194/hess-2017-288, 2017
Manuscript under review for journal Hydrol. Earth Syst. Sci.
Discussion started: 30 May 2017

At the beginning of each measurement campaign, the sensor was "nulled" according to the manufacturer's manual. Readings were taken just after each irrigation application at 1 m step, along the central line of each transect, for an overall total of 26 measurements per transect, per campaign. Taking measurements just after irrigation allowed relatively time-stable water contents to be assumed at each site throughout the monitoring campaigns.

Multi-height EM38 readings were performed at 26 locations in the middle line of each transect during the growing season. Readings were acquired at heights of 0.0, 0.2, 0.4 and 0.6 m from the ground. Overall, seven EM38 measurement campaigns were carried out during the experiment, from July 7th to September 2nd.

Just after each EM38 measurement campaign, a TDR probe was inserted vertically at the soil surface (0.0-0.25 m) in 26 sites, each corresponding to the central point of an EM38 reading. A Tektronix 1502C cable tester (Tektronix Inc., Baverton, OR) was used in this study. It enables simultaneous measurement of water content, θ, and bulk electrical conductivity, σ_b, of the soil volume explored by the probe (Heimovaara et al. 1995, Robinson and Friedman 2003, Coppola et al. 2011, Coppola et al. 2015). The TDR transmission line consisted of an antenna cable (RG58, 50 Ω characteristic impedance, 2 m long and with 0.2 Ω connector impedance) and three-wire probes, 0.25 m long, 0.07 m internal distance, and 0.005 m in diameter. The TDR probe was not embedded permanently at fixed depths along the soil profile to avoid any potential disturbance to the EMI acquisitions.

Only immediately after the last EM38 campaign (September 2nd) were TDR readings taken at three different depth intervals (0.0-0.2, 0.2-0.4, 0.4-0.6 m). After the measurements at the surface (0.0-0.2 m), a trench was dug up to 0.2 m depth. TDR probes were then inserted vertically for the additional collection of the data in the interval 0.2-0.4 m, after which the trench was deepened up to 0.4 m and readings were taken at 0.4-0.6 m. $\sigma_{b,TDR}$ readings in this last campaign were used for the calibration of the EM38 data. All the remaining six data series will be used for a validation study of the approach developed in this paper (which will be the subject of a follow-up paper).

Data Handling

Multi-height EMI readings inversion

Nonlinear 1D forward modeling, which predicts multi-height EMI readings from a loop-loop device, can be obtained by suitable simplification of Maxwell's equations that takes the symmetry of the problem into account. This approach is described in detail in (Hendrickx et al. 2002), and is based on a classical approach extensively described in the literature (Wait 1982, Ward and Hohmann 1988). The predicted data are functions of the electrical conductivity and the magnetic permeability in a homogeneously and horizontally layered medium.

When the coils of the recording device are vertically oriented with respect to the ground surface, the reading at height *h* can be expressed by using the integral:

$$-\rho^3\int_0^\infty \lambda^2 e^{-2h\lambda} R_0(\lambda) J_0(\rho\lambda)\, d\lambda, \tag{1}$$

where ρ denotes the distance between the coils, $J_0(\lambda)$ is the Bessel function of the first kind of order 0, and $R_0(\lambda)$ is a complex valued function which depends upon the electromagnetic properties of the ground layers. A similar expression is valid also when the coils are horizontally aligned. Hence the dependence of the measured data on the electrical conductivity σ_k, of the (homogeneous) j-th layer is incorporated into the function $R_0(\lambda)$. We discretize the problem with n layers whose characteristic parameters σ_j (with j = 1, . . ., n) are the unknowns we invert for. In the present research, we neglect any dependence of the electromagnetic response on magnetic permeability as we assume it is fixed and equal to the permeability of empty space. We consider two measurements for each location: one for the horizontal and one for the vertical configuration of the transmitting and receiving loops. In this way, the data used as inputs for the inversion are 2m, where m is the number of heights $h_1, h_2, \ldots, h_m$ where the measurements are performed.

A least squares data fitting approach leads to the minimization of the function:

$$f(\sigma) = \frac{1}{2}\sum_{i=1}^{2m} r_i^2(\boldsymbol{\sigma}), \tag{2}$$

where $\boldsymbol{\sigma} = (\sigma_1, \ldots, \sigma_n)^T$, and $r_i^2(\boldsymbol{\sigma})$ is the misfit between the *i-th* measurement and the corresponding forward modeling prediction based on equation (1).

We solve the nonlinear minimization problem by the inversion procedure described in Deidda, Fenu, and Rodriguez (2014). The algorithm is based on a damped regularized Gauss-Newton method. The problem is linearized at each iteration by means of a first order Taylor expansion. The use of the exact Jacobian (whose expression is detailed in Deidda, Fenu, and Rodriguez (2014) makes the computation faster and more accurate than using a finite difference approximation. The damping parameter is determined in order to ensure both the convergence of the method and the positivity of the solution. The regularized solution to each linear subproblem is computed by the truncated generalized singular value decomposition (TGSVD - Díaz de Alba and Rodriguez (2016) employing different regularization operators. Besides the classical regularization matrices based on the discretization of the first and second derivatives, to further improve the spatial resolution of EMI inversion results, we tested a nonlinear regularization stabilizer promoting the reconstruction of blocky features (Zhdanov, Vignoli, and Ueda 2006, Ley-Cooper et al. 2015, Vignoli et al. 2015, Vignoli et al. 2017). The advantage of this relatively new regularization is that, when appropriate prior knowledge about the medium to reconstruct is available, it can mitigate the smearing and over-smoothing effects of the more standard inversion strategies. This, in turn, can make the calibration of the EMI data against the TDR data more effective. For this reason, in the following, the EMI results used for our assessments are those inferred by means of this sharp regularization. The differences between the "standard" smooth (based on the first derivative) reconstruction and the sharp one are clearly shown in Figure 2.

It is worth noting that the constant magnetic permeability assumption is not always valid: inverting for the magnetic permeability is sometimes not only necessary, but can also provide an additional tool for soil characterization (Deidda, Diaz De Alba, and Rodriguez 2017).

For the sake of clarity, hereafter, the σ_b values generated from the EMI data inversion will be identified explicitly as $\sigma_{b,EMI}$.

TDR-based water content and bulk electrical conductivity

The Tektronix 1502C can measure the total resistance, R_t, of the transmission line by:

$$R_t = Z_c \frac{(1+\rho_\infty)}{(1-\rho_\infty)} = R_s + R_c \tag{3}$$

where R_s is the soil's contribution to total resistance and R_c accounts for the contribution of the series resistance from the cable, the connector, Z_c, is the characteristic impedance of the transmission line, and ρ is a reflection coefficient at a very long time, when the waveform has stabilized.

The σ_b value at 25°C can be calculated as (Rhoades and van Schilfgaarde 1976, Wraith et al. 1993):

$$\sigma_{b\,25^\circ C} = \frac{K_c}{Z_c} f_T \tag{4}$$

where K_c is the geometric constant of the TDR probe and f_T is a temperature correction factor to be used for values recorded at temperatures other than 25°C. Both Z_c and K_c can be determined by measuring R_t with the TDR probe immersed in a solution with known conductivity σ_b. Hereafter, these σ_b measurements will be identified as $\sigma_{b,TDR}$.

Evaluation of Concordance between $\sigma_{b,TDR}$ measurements and $\sigma_{b,EMI}$ estimates

The agreement between $\sigma_{b,TDR}$ measurements and $\sigma_{b,EMI}$ estimations in the 0.0-0.20 m layer was evaluated by the Concordance Correlation Coefficient, ρ_L :

$$\rho_L = \frac{2s_{xy}}{z_x^2 + z_y^2 + (m_x - m_y)^2} \tag{5}$$

where m_x, m_y, s_x, s_y, s_{xy} are means, standard deviations and covariances of the two data series ($x = \sigma_{b,EMI}$; $y = \sigma_{b,TDR}$), respectively.

Scatter plots of the $\sigma_{b,EMI}$ and $\sigma_{b,TDR}$ data series (both original and filtered) for the depth interval 0.0-0.20 m were evaluated by the line of perfect concordance (1:1 line) and the reduced major axis of the data (RMA) (Freedman et al. 1991). The method combines measurements of both precision and accuracy to determine how close the two data series are to the line of perfect concordance $\sigma_{b,EMI} = \sigma_{b,TDR}$. Compared to the classical Pearson correlation coefficient, ρ_P:

$$\rho_P = \frac{s_{xy}}{s_x s_y}, \tag{6}$$

ρ_L not only measures the strength of linear relationship (how close the data in the scatter plot are to a line), but also the level of agreement (how close that line is to the line of perfect agreement, the 1:1 line). In this sense, ρ_L may also be calculated as (Cox 2006):

Hydrology and Earth System Sciences
Open Access
Discussions

$$\rho_L = \rho_P C_b,$$
$$C_b = \frac{2}{\left(v + 1/v + u^2\right)}, \tag{7}$$
$$v = s_x / s_y,$$

and

$$u = \left(m_x - m_y\right) / \sqrt{s_x s_y},$$

where C_b is the bias correction factor measuring how far the best-fit line deviates from the 1:1 line. The maximum value of C_b = 1 (0<C_b<1) corresponds to no deviation from the line. The smaller C_b is, the greater the deviation from the line. In other words, C_b is a measure of accuracy (how much the average estimate differs from the average measurement value, assumed to be the true value) and refers to the systematic error, whereas ρ_P is a measure of precision (measures the variability of measurements around their own average) and refers to the random error. The RMA line is given by:

$$y = \left(m_y - \beta m_x\right) + \beta x = \alpha + \beta x. \tag{8}$$

This line passes through the means of the x and y values and has slope given by the sign of Pearson's correlation coefficient, ρ_P, and the ratio of the standard deviations, s, of the two series (Freedman et al. 1991, Corwin and Lesch 2005):

$$\beta = s_y / s_x. \tag{9}$$

ρ_L increases in value as (i) the RMA approaches the line of perfect concordance (a matter of accuracy) and (ii) the data approach the RMA (a matter of precision). In the ideal case of perfect concordance, the intercept of the RMA, α, should be 0 and β should be 1. Therefore, α ≠ 0 or β ≠ 1 indicate additive and/or multiplicative biases (location and/or scale shifts). The concordance was evaluated for the original TDR data, as well as for the filtered TDR data. For the analysis carried out in the results section, it is worth noting here that the coefficients α and β depend only on the statistical characteristics (mean and standard deviation) of the two series, as $\alpha = m_y - \beta m_x$ and $\beta = s_y / s_x$.

Fourier filtering

Because of their relatively small observation volume (≈ 10^{-3} m^3), TDR sensors provide quasi-pointlike measurements and are thus more effective in capturing small-scale variability (in water content, solute concentrations) induced by natural soil heterogeneity. Thus the variability within a set of TDR readings is expected to originate from a combination of small and large-scale heterogeneities (high and low spatial frequency components). By contrast, the EMI measurements (because of the size and physics of the instrumentation) necessarily integrate out the small-scale variability at the TDR scale of investigation.

Hence, in order to make the two datasets comparable, the original spatial TDR data series need to be filtered to remove the variation from small-scale heterogeneities (recorded only by the TDR probe). In this way, only the information at a spatial scale equal to or larger than the observation volume of both sensors is preserved.

Hydrol. Earth Syst. Sci. Discuss., doi:10.5194/hess-2017-288, 2017
Manuscript under review for journal Hydrol. Earth Syst. Sci.
Discussion started: 30 May 2017

Hydrology and Earth System Sciences
Open Access
Discussions

The Fourier transform (FT) of discrete stationary series of length M equispaced at intervals Δp (x_p, p=0,1,…,M-1) (where x is the variable, and p the spatial or temporal location on the series) is defined as (Shumway 1988):

$$X(k)=M^{-1}\sum_{s=0}^{M-1}\left(x_p-\bar{x}\right)\exp\left(-2\pi i v_k p\right), \tag{10}$$

where k= 0,1….,M-1, X(k) are the Fourier coefficients, i= $\sqrt{-1}$, v_k = k/M is the wave number (or frequency) in cycles per unit distance (or time) and $\bar{x}$ is the sample mean. If the series is detrended, x_p in equation (22) is the detrended series.

The FT in equation (10) may be written in terms of sine and cosine transform, noting that:

$$\exp\left(-2\pi i v_k p\right)=\cos\left(-2\pi v_k p\right)-i\sin\left(-2\pi v_k p\right) \tag{11}$$

Thus equation (10) becomes:

$$X(k)=X_C(k)-iX_S(k) \tag{12}$$

The Fourier coefficients X(k) are complex numbers. Most software packages (e.g., MatLab, SAS, Microsoft Excel) have built-in Fast Fourier transform (FFT) algorithms that considerably speed up the computation of equation (10); the sine and cosine transforms are immediately available from the real and imaginary parts of the computed X(k).

By using the following coefficients:

$$\begin{aligned} a_k &= -\frac{2}{M}\mathrm{imag}(X(k)), \quad 0<k<\frac{M}{2}; \\ b_k &= -\frac{2}{M}\mathrm{real}(X(k)), \quad 0<k<\frac{M}{2}, \end{aligned} \tag{13}$$

it is easy to perform the inverse FT and recover the original signal:

$$x(p)=a_0+\sum_{k=0}^{(M-1)/2}\left(a_k\sin\left(2\pi v_k p\right)+b_k\cos\left(2\pi v_k p\right)\right) \tag{14}$$

Equation (14) is central to the filtering approach we use in the present paper. It can be used to reconstitute a smoothed data series by retaining selected harmonics alone (e.g., only the low frequency harmonics). The frequencies to be selected can be identified by examining the power spectral density - see equation (16) below - of the data series.

The periodogram can be written as the squared modulus of the FT:

$$P_x\left(v_k\right)=\left|X(k)\right|^2=\left[X_C^2(k)+X_S^2(k)\right]=X(k)\overline{X(k)}, \tag{15}$$

where the overbar denotes complex conjugate. P_x is an asymptotically unbiased estimator for the spectrum (Shumway 1988). It is common practice to average adjacent values of the periodogram to obtain estimates with more degrees of freedom, and create a smoothed power spectrum. The average spectral estimator, in a frequency interval centered on v_k, is defined as:

$$f_x^{P,B}\left(v_k\right)=L^{-1}\sum_{l=-(L-1)/2}^{(L-1)/2}P\left(v_k+\frac{l}{M}\right)=L^{-1}\sum_{l=-(L-1)/2}^{(L-1)/2}\left|X(k+l)\right|^2, \tag{16}$$

where L is some odd integer considerably smaller than M and defining the size of the averaging window. Hence, the averaging window is characterized by a bandwidth B = L/M (cycles per point) centered on ν_k. $f_x^{P,B}(\nu_k)$ is the periodogram-based power spectrum averaged on B and with, approximately, a chi-squared distribution, in which the degrees of freedom depend on the width L of the window used.

The 100(1-α) confidence interval for the smoothed spectrum can be calculated as:

$$\frac{2Lf_x^{P,B}(\nu_k)}{\chi^2_{2L}(a/2)} \le f_x^n(\nu_k) \le \frac{2Lf_x^{P,B}(\nu_k)}{\chi^2_{2L}(1-a/2)}, \tag{17}$$

where α is the significance level and $f_x^n(\nu_k)$ is the background noise power spectrum. The null hypothesis is $f_x^{P,B}(\nu_k)=f_x^n(\nu_k)$ vs. $f_x^{P,B}(\nu_k)\neq f_x^n(\nu_k)$. If $f_x^n(\nu_k)$ falls within the interval in equation (17), we fail to reject the hypothesis. If not, the estimated power spectrum at a given frequency ν_k has to be considered significantly different from that of the assumed background noise. In the case of white noise, implying a uniform distribution of the power spectrum across frequencies, $f_x^n(\nu_k)$ can be considered as the mean of all power spectrum estimates.

Results and Discussion

Hereafter, the original and filtered data will be respectively labeled ORG and FLT. The graphs in panel (a) of Figures 3, 4 and 5 compare $\sigma_{b,TDR}$ measured by TDR against the corresponding conductivity $\sigma_{b,EMI}$ retrieved by the EMI (sharp) inversion, respectively, for the layers at 0-0.20, 0.20-0.40, and 0.40-0.60 m. From the left, the graphs refer respectively to the transects identified as 100-6dS, 50-6dS, 100-1dS and 50-1dS. All the plots report the line of perfect concordance (1:1, black line) and the main regression axis (MRA, red line).

The general outcome is that, in all four transects, and for all three considered depth-layers, the $\sigma_{b,EMI}$ values underestimate the $\sigma_{b,TDR}$ measurements, such that the MRA line generally lies above the 1:1 line. Not surprisingly, the EMI result seems quite insensitive to TDR variability. Also, a considerable scatter around the MRA line may be observed for all four transects.

Tables 1, 2 and 3 show the MRA coefficients (C_b, α , β), as well as the Pearson, ρ_P, and the concordance correlation, ρ_L, for the three depth-layers and for all four transects investigated. We recall that the bias correction factor, C_b, the slope, β, and the intercept, α, should be respectively close to 1, 1 and 0, for the MRA to approximate the line of perfect concordance. For all the transects and all the depth-layers considered, the parameters confirm the relatively loose relationship between $\sigma_{b,EMI}$ and $\sigma_{b,TDR}$ already observed in the graphs, both in terms of accuracy (the distance of the MRA line from the 1:1) and precision (the data scatter around the MRA line).

von Hebel et al. (2014) found a similar behavior when comparing their EMI and ERT datasets. In that case, the EC_a values measured by EMI systematically underestimated the EC_a generated by applying EMI forward modeling to the σ_b distribution retrieved by ERT. To remove the bias, the authors simply performed a linear regression between measured and predicted ECa after applying a ten-term moving average to the original data. By using the regression coefficients, all the measured EC_a values were converted to ERT-calibrated EC_a values.

Here, we follow a different approach to calibrate the $\sigma_{b,EMI}$ values against the $\sigma_{b,TDR}$ measurements based on the MRA coefficients and hence on the statistical parameters (mean and standard deviation) of the two data series. Specifically, the present approach looks for a systematic correction of the bias based on well-defined statistical sources of the discrepancies. In short, the proposed method performs the calibration in the σ_b model-space, instead of the EC_a data-space.

Our model-space approach mostly relies on the statistical parameters of the two series. Analyzing the role of these statistics in explaining the discrepancies between EMI and TDR data observed in Figures 3-5 may help to understand how they can be exploited for converting EMI measurements to TDR values.

In nearly all of the graphs in panel (a) of Figures 3-5, the discrepancies between $\sigma_{b,EMI}$ and $\sigma_{b,TDR}$ values can be decomposed in the following components:

1. The distance along the $\sigma_{b,EMI}$ axis of the MRA line from the 1:1 line, that is the difference between the $\sigma_{b,EMI}$ and the $\sigma_{b,TDR}$ means.

2. The difference in the slope of the MRA and of the 1:1 lines, which stems from the different variability of $\sigma_{b,EMI}$ (its standard deviation) and that of $\sigma_{b,TDR}$. We recall here that the slope of the MRA is just the ratio of the two standard deviations, $\hat{\beta} = s_y / s_x$.

3. The scatter of the data around the MRA line, which may come from different sensors' noise and the influence of surrounding conditions (e.g., temperature).

Below, we analyze in detail the role of all these three points with the support of the measured data.

1. The distance of the MRA from the 1:1 line may be mostly ascribed to the difference in the observed means. The graph in Figure 6a compares the means for the two original series (open squares-solid line for TDR, open circles-dashed line for EMI). The plot in Figure 6b reports the same comparison on a 1:1 plot (open triangles-solid regression line). The means confirm the general underestimation of TDR by the EMI data. However, the trends are evidently similar, which is reflected in the high correlation between the means of the two series, with a significantly high R^2=0.81. The high correlation of the means has very positive implications from an applicative point of view, as, after calibration in a specific soil, it allows the TDR mean to be inferred given the mean of EMI readings taken in that soil, and thus gives us the possibility to transpose the more reliable TDR information across the larger area that can be practically investigated with EMI.

2. The different slope of the two lines has to be ascribed to the different variability of the two series. The graph in Figure 7a compares the standard deviations for the two original series (open squares-solid line for TDR, open circles-dashed line for EMI). The graph in figure 7b reports the same comparison on a 1:1 plot (open triangles-solid regression line). Conceptually, the different variability of the two series may well be related to the different sensor observation volumes (coming from the different spatial sensitivity of the sensors) (Coppola et al. 2016). For TDR probes, most of the measurement sensitivity is close to the rods (Ferre et al. 1998). Conversely, the spatial resolution of inverted EMI ECa values may be much lower as the

Hydrol. Earth Syst. Sci. Discuss., doi:10.5194/hess-2017-288, 2017
Manuscript under review for journal Hydrol. Earth Syst. Sci.
Discussion started: 30 May 2017

Hydrology and Earth System Sciences
Discussions

resolution of the EMI result depends on the physics of the method, the specifications (and configuration) of the recording device, and the regularization type applied during inversion. That said, the EMI is generally unable to capture the small-scale variability seen by the TDR. For our calibration purposes, it is important to make the variability of EMI and TDR conductivities actually comparable. As discussed by Coppola et al. (2016), a method can be to filter the high frequency component (at small spatial scale) of the original TDR data, while retaining the lower frequency information, that is information at a spatial scale larger than the observation volume of the TDR sensor and attuned with the resolution of the EMI distribution values coming from the inversion. From a practical point of view, this makes sense, as TDR readings are often "too local" to actually represent the macroscopic physical characteristics of interest for applications (water content, solute concentrations). The volume explored by a TDR probe may, or may not, include preferential channels (Mallants et al. 1994, Oberdörster et al. 2010), stones (Coppola et al. 2011, Coppola et al. 2013), small-scale changes in the texture and structure (Coppola et al. 2011), which can make the interpretation of local measurements difficult for practical applications. In this sense, EMI's removal of these small-scale effects may be desirable from a management perspective.

Accordingly, original TDR data were conditioned via Fourier filtering, as described in the Material and Methods section. The number of low-frequency harmonics to be used for rebuilding the filtered signal was selected according to the spectrum for each depth and transect - see equation (16) - and, in general, it was included in three-six harmonics. The filtering results, in terms of standard deviations, are reported in figure 7a (crosses-dashed line) and in figure 7b (open squares-dashed regression line). As expected, filtering made the standard deviations much closer (almost overlapping in many cases) for all transects and for all considered depth-layers. The regression improved significantly from 0.25 for the original data to 0.78 when TDR data were filtered. As with the means, the high correlation of the standard deviations has positive implications from a practical point of view: it allows the TDR standard deviation to be inferred, given the standard deviation of EMI readings taken in that soil. Panel b of Figures 3 to 5 shows the comparison of the original EMI and filtered TDR data. The concordance coefficients in the case of filtered TDR data are again reported in Tables 1 to 3. Obviously, because of the almost overlapping EMI and TDR standard deviations after filtering, the MRA line turned out to be much more parallel to the 1:1 line, as indicated by the coefficient β, which is now much closer to 1.

3. In general, however, filtering left the scatter around the MRA line almost unaltered. Here the scatter was zeroed by again using the intercept and the slope coefficients of the MRA obtained after TDR filtering. Specifically, the filtered TDR data were recalculated from the original EMI data as:

$$\sigma^{rg}_{b,TDR(FLT)} = \alpha + \beta\sigma_{b,EMI} \qquad (18)$$

The superscript *rg* means filtered data after regression. The results are again reported in panel c of figures 3-5. As an example of the calibration results, figure 8 compares the maps of bulk electrical conductivity for the 100-6dS transect obtained respectively by plotting the original

$\sigma_{b,EMI}$ (figure 8a) coming from the inversion of the EMI signal and the calibrated $\sigma^{rg}_{b,TDR(FLT)}$ (figure 8b) obtained by applying the equation 18 to the $\sigma_{b,EMI}$ data of the first map. After calibration, the nearly homogeneous σ_b distribution represented in the map of figure 8a, coming from the substantial insensitivity of the original EMI data to TDR variability, turn into a physically more plausible σ_b layering, largely reproducing the true one observed by the TDR probes .

All the points discussed above provide the rationale to deduce the TDR-FLT data based on the statistical parameters of the EMI and TDR data (m_x, m_y, s_x, s_y). Summarizing, the procedure requires the following steps:

1. Filtering the TDR data, by retaining only the low-frequency part of the signal. The number of harmonics to be selected depends on the length of the data series, as well as on the spectrum characteristics. This step will make the standard deviations of the two data series similar, thus turning the data parallel to the 1:1 line;
2. Using the average (m_x, m_y) and the standard deviation (s_x, s_y) of the original $\sigma_{b,EMI}$ EMI data and of the filtered $\sigma_{b,TDR(FLT)}$ TDR data to calculate the MRA line coefficients as $\alpha = m_y - \beta m_x$ and $\beta = s_y / s_x$. Of course, the averages for the original and the filtered TDR data will coincide;
3. Straightening the data on the MRA line (zeroing the scatter) by recalculating the TDR-FLT data from the original EMI data and the MRA coefficients $\sigma^{rg}_{b,TDR(FLT)} = \alpha + \beta\sigma_{b,EMI}$.

As already discussed, the high correlation of the means and the standard deviations of the two series are central for this procedure to be of practical interest. To explain this with an example, let us assume an experiment (like that described herein) has been carried out in a calibration field within the area to be monitored by an EMI sensor; the experiment would allow regressions to be built for the mean and the standard deviation of the original EMI and the filtered TDR, like those shown in figures 6b and 7b.

Now let us take a set of ECa readings in the area to be monitored. After inversion, these ECa data provide a set of $\sigma_{b,EMI}$ values. For the reasons discussed above, we know that these values do not represent the actual values one would measure directly by using a TDR probe. Rather, they only contain the low-frequency information supplied by TDR (most likely, together with some shifts connected with the poor absolute calibration of the EMI system and/or the working conditions, e.g., the temperature). We now have a workflow to convert these $\sigma_{b,EMI}$ data into the corresponding filtered TDR values. In other words, the proposed workflow enables us to translate the original non-calibrated $\sigma_{b,EMI}$ data into the actual σ_b we would collect in ideal conditions, and which would perfectly match "low-resolution" TRD measurements. The workflow requires:

1. The mean and the standard deviation of EMI, which can be calculated by the $\sigma_{b,EMI}$ data;
2. The mean and the standard deviation of filtered TDR, which can be calculated by the regressions from the calibration experiment (as in figures 6b and 7b);

These statistics may now be used to evaluate coefficients α and β to be used in equation (18) to convert the original $\sigma_{b,EMI}$ data into as many $\sigma^{rg}_{b,TDR(FLT)}$ values. Hence, $\sigma^{rg}_{b,TDR(FLT)}$ is our best possible estimation of the true electrical conductivity at the scale of investigation of the EMI survey: it is the original $\sigma_{b,EMI}$ after the application of the appropriate rescaling and shifts deduced by the more reliable and absolutely calibrated TDR measurements.

Conclusions

The objective of the paper was to infer the bulk electrical conductivity distribution in the root zone from multi-height (potentially non-calibrated) EMI readings. TDR direct measurements were used as ground-truth σ_b data to evaluate the correctness of the σ_b estimations generated by EMI inversion. For all four transects and for all three depth-layers considered in this study, the $\sigma_{b,EMI}$ values underestimate the $\sigma_{b,TDR}$ measurements, such that the MRA line generally lies above the 1:1 line. Also, a considerable scatter around the MRA line was observed for all four transects.

The proposed analysis allowed discussion of the physical reasons for the differences between EMI- and TDR-based electrical conductivity and develop an approach to calibrate the original $\sigma_{b,EMI}$ by using the $\sigma_{b,TDR}$ measurements. Our approach is based on the MRA coefficients and hence on the statistical parameters (mean and standard deviation) of the two series. Specifically, the approach looks for a systematic correction of the bias based on well-defined statistical sources of the discrepancies. A significant high correlation was found for the means and the standard deviations of the two series, especially after filtering the TDR data. This is crucial for the practical application of our methodology.

The proposed strategy lies in the fact that TDR direct measurements supply absolutely calibrated observations of the electrical conductivity of the soil and hence can be effectively used to calibrate the conductivity distributions inferred from EMI data. The availability of EMI calibrated data paves the way to reliable reconstructions of the electrical conductivity distribution over large areas (typical for EMI surveys, but not for TDR campaigns) unaffected by the usual EMI miscalibrations. This, in turn, can result in the possibility of effective time-lapse surveys and/or in consistent merging of subsequent surveys (at any time the dynamic components of the system under investigation can be neglected).

On the other hand, the proposed statistical workflow for making the TDR measurement comparable with the associated EMI results provides a more sophisticated approach than simple smoothing to upscale the TDR data. Thus, from the opposite perspective, the approach in question can be used to tackle the problems connected with handling the TDR data characterized by excessively high spatial resolution.

Finally, the approach used here allows TDR calibration measurements to be used not necessarily at the same sites and in the same quantities as EMI readings, as it is based on means and standard deviations and does not require site-by-site data comparison.

References

Abdu, H., D.A. Robinson, and S.B. Jones. 2007. Comparing bulk soil electrical conductivity determination using the DUALEM-1S and EM38-DD electromagnetic induction instruments. *Soil Sci. Soc. Am. J.* 71 (1):189-196. doi: 10.2136/sssaj2005.0394.

Amezketa, E. 2006. An integrated methodology for assessing soil salinization, a pre-condition for land desertification. *J. Arid Environ.* 67 (4):594-606. doi: 10.1016/j.jaridenv.2006.03.010.

Borchers, B., T. Uram, and J.M.H. Hendrickx. 1997. Tikhonov regularization of electrical conductivity depth profiles in field soils. *Soil Sci. Soc. Am. J.* 61 (4):1004-1009. doi: 10.2136/sssaj1997.03615995006100040002x.

Coppola, A., G. Dragonetti, A. Comegna, N. Lamaddalena, B. Caushi, M.A. Haikal, and A. Basile. 2013. Measuring and modeling water content in stony soils. *Soil Till. Res*. 128:9-22.

Coppola, A., K. Smettem, A. Ajeel, A. Saeed, G. Dragonetti, A. Comegna, N. Lamaddalena, and A. Vacca. 2016. Calibration of an electromagnetic induction sensor with time-domain reflectometry data to monitor rootzone electrical conductivity under saline water irrigation. *Eur. J. of Soil Sci.* 67 (6):737-748. doi: 10.1111/ejss.12390.

Coppola, A., N. Chaali, G. Dragonetti, N. Lamaddalena, and A. Comegna. 2015. Root uptake under non-uniform root-zone salinity. *Ecohydrology*. 8 (7):1363-1379. doi: 10.1002/eco.1594.

Coppola, A., A. Comegna, G. Dragonetti, M. Dyck, A. Basile, N. Lamaddalena, M. Kassab, and V. Comegna. 2011. Solute transport scales in an unsaturated stony soil. *Adv. Water Resour*. 34 (6):747-759. doi: http://dx.doi.org/10.1016/j.advwatres.2011.03.006.

Corwin, D.L., and S.M. Lesch. 2005. Apparent soil electrical conductivity measurements in agriculture. *Comput. Electron. Agr.* 46 (1):11-43.

Cox, N.J. 2006. Assessing agreement of measurements and predictions in geomorphology. *Geomorphology*. 76 (3):332-346.

Deidda, G.P., E. Bonomi, and C. Manzi. 2003. Inversion of electrical conductivity data with Tikhonov regularization approach: some considerations. *Ann. Geophys*.

Deidda, G.P., C. Fenu, and G. Rodriguez. 2014. Regularized solution of a nonlinear problem in electromagnetic sounding *Inverse Probl*. 30 (12):125014.

Deidda, G.P., P. Diaz De Alba, and G. Rodriguez. 2017. Identifying the magnetic permeability in multi-frequency EM data inversion. *Submitted*.

Díaz de Alba, P., and G. Rodriguez. 2016. Regularized Inversion of Multi-Frequency EM Data in Geophysical Applications. In *Trends in Differential Equations and Applications*, 357-369. Springer.

Doolittle, J.A., and E.C. Brevik. 2014. The use of electromagnetic induction techniques in soils studies. *Geoderma* . 223:33-45.

Ferre, P.A., J.H. Knight, D.L. Rudolph, and R.G. Kachanoski. 1998. The sample areas of conventional and alternative time domain reflectometry probes. *Water Resour. Res*. 34 (11):2971-2979.

Fiandaca, G., J. Doetsch, G. Vignoli, and E. Auken. 2015. Generalized focusing of time-lapse changes with applications to direct current and time-domain induced polarization inversions. *Geophys. J. Int*. 203 (2):1101-1112. doi: 10.1093/gji/ggv350.

Freedman, D., R. Pisani, R. Purves, and A. Adhikari. 1991. Statistics (2nd ed.). New York: W. W. Norton.

Gebbers, R., E. Lück, M. Dabas, and H. Domsch. 2009. Comparison of instruments for geoelectrical soil mapping at the field scale. *Near Surf. Geophys*. 7 (3):179-190. doi: 10.3997/1873-0604.2009011

Günther, T. 2011. Timelapse ERT inversion approaches and their applications. *Geoelectric Monitoring*:91.

Heimovaara, T.J., A.G. Focke, W. Bouten, and J.M. Verstraten. 1995. Assessing temporal variations in soil water composition with time domain reflectometry. *Soil Sci. Soc. Am. J.* 59 (3):689-698. doi: 10.2136/sssaj1995.03615995005900030009x.

Hendrickx, J.M.H., B. Borchers, D.L. Corwin, S.M. Lesch, A.C. Hilgendorf, and J. Schlue. 2002. Inversion of soil conductivity profiles from electromagnetic induction measurements. *Soil Sci. Soc. Am. J.*. 66 (3):673-685. doi: 10.2136/sssaj2002.6730.

Lavoué, F., J. van der Kruk, J. Rings, F. André, D. Moghadas, J.A. Huisman, S. Lambot, L. Weihermüller, J. Vanderborght, and H. Vereecken. 2010. Electromagnetic induction calibration using apparent electrical conductivity modelling based on electrical resistivity tomography. *Near Surf. Geophys*. 8 (6):553-561.

Lesch, S.M., J.D. Rhoades, L.J. Lund, and D.L. Corwin. 1992. Mapping soil salinity using calibrated electromagnetic measurements. *Soil Sci. Soc. Am. J.*. 56 (2):540-548. doi: 10.2136/sssaj1992.03615995005600020031x.

Ley-Cooper, A.Y., A. Viezzoli, J. Guillemoteau, G. Vignoli, J. Macnae, L. Cox, and T. Munday. 2015. Airborne electromagnetic modelling options and their consequences in target definition. *Explor. Geophys*. 46 (1):74-84. doi: 10.1071/eg14045.

Lin, K. 1989. A concordance correlation coefficient to evaluate reproducibility. *Biometrics*:255-268.

Mallants, D., M. Vanclooster, M. Meddahi, and J. Feyen. 1994. Estimating solute transport in undisturbed soil columns using time-domain reflectometry. *Journal Contam. Hydrol*. 17 (2):91-109. doi: 10.1016/0169-7722(94)90016-7.

McNeill, J.D. 1980. Electromagnetic terrain conductivity measurement at low induction numbers. Geonics Limited Ontario, Canada.

Mester, A., J. Van Der Kruk, E. Zimmermann, and H. Vereecken. 2011. Quantitative Two-Layer Conductivity Inversion of Multi-Configuration Electromagnetic Induction Measurements. *Vadose Zone J*. 10:1319-1330. doi: 10.2136/vzj2011.0035.

Minsley, B.J., B.D. Smith, R. Hammack, J.I. Sams, and G. Veloski. 2012. Calibration and filtering strategies for frequency domain electromagnetic data. *J. Appl. Geophys*. 80:56-66. doi: 10.1016/j.jappgeo.2012.01.008.

Moghadas, D., F. André, J.H. Bradford, J. van der Kruk, H. Vereecken, and S. Lambot. 2012. Electromagnetic induction antenna modelling using a linear system of complex antenna transfer functions. *Near Surf. Geophys*. 10 (3):237-247. doi: 10.3997/1873-0604.2012002

Nüsch, A.K., P. Dietrich, U. Werban, T. Behrens, and N. Prakongkep. 2010. Acquisition and reliability of geophysical data in soil science. Paper read at 19th world congress of soil science, soil solutions for a changing world, Brisbane, Australia.

Oberdörster, C., J. Vanderborght, A. Kemna, and H. Vereecken. 2010. Investigating preferential flow processes in a forest soil using time domain reflectometry and electrical resistivity tomography. *Vadose Zone J*. 9 (2):350-361.

Pagliara, G., and G. Vignoli. 2006. Focusing inversion techniques applied to electrical resistance tomography in an experimental tank. In *XI International Congress of the International Association for Mathematical Geology*.

Rhoades, J.D., and D.L. Corwin. 1981. Determining soil electrical conductivity-depth relations using an inductive electromagnetic soil conductivity meter. *Soil Sci. Soc. Am. J.*. 45 (2):255-260.

Rhoades, J.D., and J. van Schilfgaarde. 1976. An electrical conductivity probe for determining soil salinity. *Soil Sci. Soc. Am. J.* 40 (5):647-651. doi: 10.2136/sssaj1976.03615995004000050016x.

Robinson, D.A., and S.P. Friedman. 2003. A method for measuring the solid particle permittivity or electrical conductivity of rocks, sediments, and granular materials. *J. Geophys. Res-Sol Ea*. 108 (B2):2076. doi: 10.1029/2001JB000691.

Robinson, D.A., I. Lebron, S.M. Lesch, and P. Shouse. 2004. Minimizing Drift in Electrical Conductivity Measurements in High Temperature Environments using the EM-38. *Soil Sci. Soc. Am. J.*. 68 (2):339-345. doi: 10.2136/sssaj2004.3390.

Robinson, D.A., H. Abdu, I. Lebron, and S.B. Jones. 2012. Imaging of hill-slope soil moisture wetting patterns in a semi-arid oak savanna catchment using time-lapse electromagnetic induction. *J. Hydrol*. 416–417:39-49. doi:https://doi.org/10.1016/j.jhydrol.2011.11.034.

Santos, F.A. Monteiro, J. Triantafilis, K.E. Bruzgulis, and J.A.E. Roe. 2010. Inversion of Multiconfiguration Electromagnetic (DUALEM-421) Profiling Data Using a One-Dimensional Laterally Constrained Algorithm. *Vadose Zone J*. 9:117-125. doi: 10.2136/vzj2009.0088.

Sheets, K.R., and J.M.H. Hendrickx. 1995. Noninvasive soil water content measurement using electromagnetic induction. *Water Resour. Res*. 31 (10):2401-2409.

Shumway, R.H. 1988. *Applied Time Series Analysis*: Prentice-Hall, Englewood Cliffs, NJ.

Sudduth, K.A., S.T. Drummond, and N.R. Kitchen. 2001. Accuracy issues in electromagnetic induction sensing of soil electrical conductivity for precision agriculture. *Comput. Electron. Agr*. 31 (3):239-264. doi: 10.1016/S0168-1699(00)00185-X.

Triantafilis, J., G.M. Laslett, and A.B. McBratney. 2000. Calibrating an electromagnetic induction instrument to measure salinity in soil under irrigated cotton. *Soil Sci. Soc. Am. J*. 64 (3):1009-1017. doi: 10.2136/sssaj2000.6431009x.

Vignoli, G., G. Fiandaca, A.V. Christiansen, C. Kirkegaard, and E. Auken. 2015. Sharp spatially constrained inversion with applications to transient electromagnetic data. *Geophys. Prospect*. 63 (1):243-255.

Vignoli, G., V. Sapia, A. Menghini, and A. Viezzoli. 2017. Examples of Improved Inversion of Different Airborne Electromagnetic Datasets Via Sharp Regularization. *J. Environ. Eng. Geophys.* 22 (1):51-61. doi: 10.2113/jeeg22.1.51.

Vignoli, G., R. Deiana, and G. Cassiani. 2012. Focused inversion of vertical radar profile (VRP) traveltime data. *Geophysics*. 77 (1):H9-H18. doi: 10.1190/geo2011-0147.1.

von Hebel, C., S. Rudolph, A.Mester, J.A. Huisman, P. Kumbhar, H. Vereecken, and J. van der Kruk. 2014. Three-dimensional imaging of subsurface structural patterns using quantitative large-scale multiconfiguration electromagnetic induction data. *Water Resour. Res*. 50 (3):2732-2748.

Wait, J.R. 1982. Geo-Electromagnetism. In *Geo-Electromagnetism*, 1-67. Academic Press.

Ward, S.H., and G.W. Hohmann. 1988. Electromagnetic theory for geophysical applications. *Electromagnetic methods in applied geophysics.*

Wraith, J.M., B.L. Woodbury, W.P. Inskeep, and S.D. Comfort. 1993. A simplified waveform analysis approach for monitoring solute transport using time-domain reflectometry. *Soil Sci. Soc. Am. J*. 57 (3):637-642.

Yao, R., and Jingsong Y. 2010. Quantitative evaluation of soil salinity and its spatial distribution using electromagnetic induction method. *Agr. Water Manage*. 97 (12):1961-1970. doi: 10.1016/j.agwat.2010.02.001.

Yu, M., and D.E. Dougherty. 2000. Modified total variation methods for three-dimensional electrical resistance tomography inverse problems. *Water Resour. Res*. 36 (7):1653-1664.

Zhdanov, M.S., G. Vignoli, and T. Ueda. 2006. Sharp boundary inversion in crosswell travel-time tomography. *J. Geophys. Eng*. 3 (2):122.

Zhdanov, M.S. 2002. Methods in Geochemistry and Geophysics, edited by S. Zhdanov Michael, xix-xxiii. Elsevier.

Hydrol. Earth Syst. Sci. Discuss., doi:10.5194/hess-2017-288, 2017
Manuscript under review for journal Hydrol. Earth Syst. Sci.
Discussion started: 30 May 2017

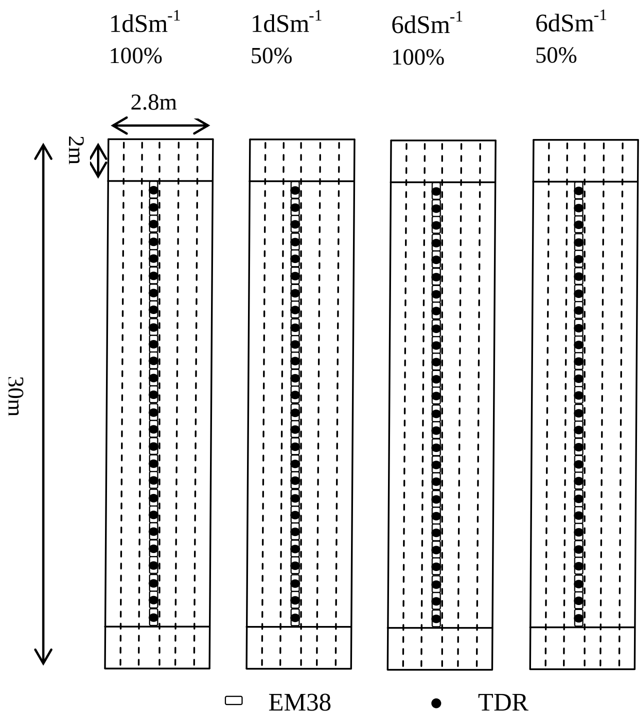

Figure 1. Schematic view of the experimental field

Hydrol. Earth Syst. Sci. Discuss., doi:10.5194/hess-2017-288, 2017
Manuscript under review for journal Hydrol. Earth Syst. Sci.
Discussion started: 30 May 2017

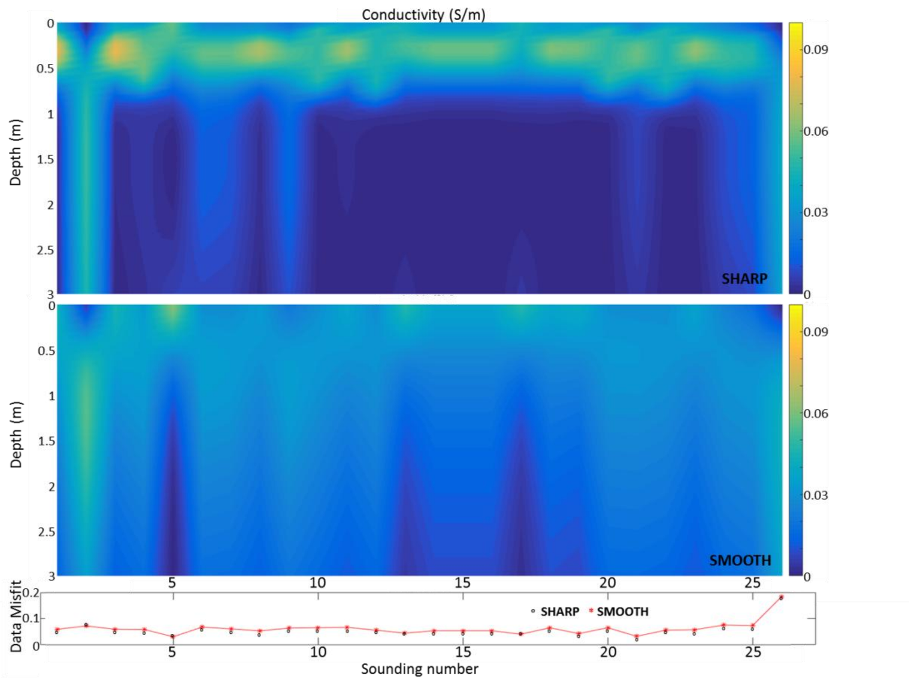

Figure 2. Examples of sharp and smooth inversions applied to the same dataset 100-6dS. The results are shown together with their corresponding data misfit

Hydrol. Earth Syst. Sci. Discuss., doi:10.5194/hess-2017-288, 2017
Manuscript under review for journal Hydrol. Earth Syst. Sci.
Discussion started: 30 May 2017

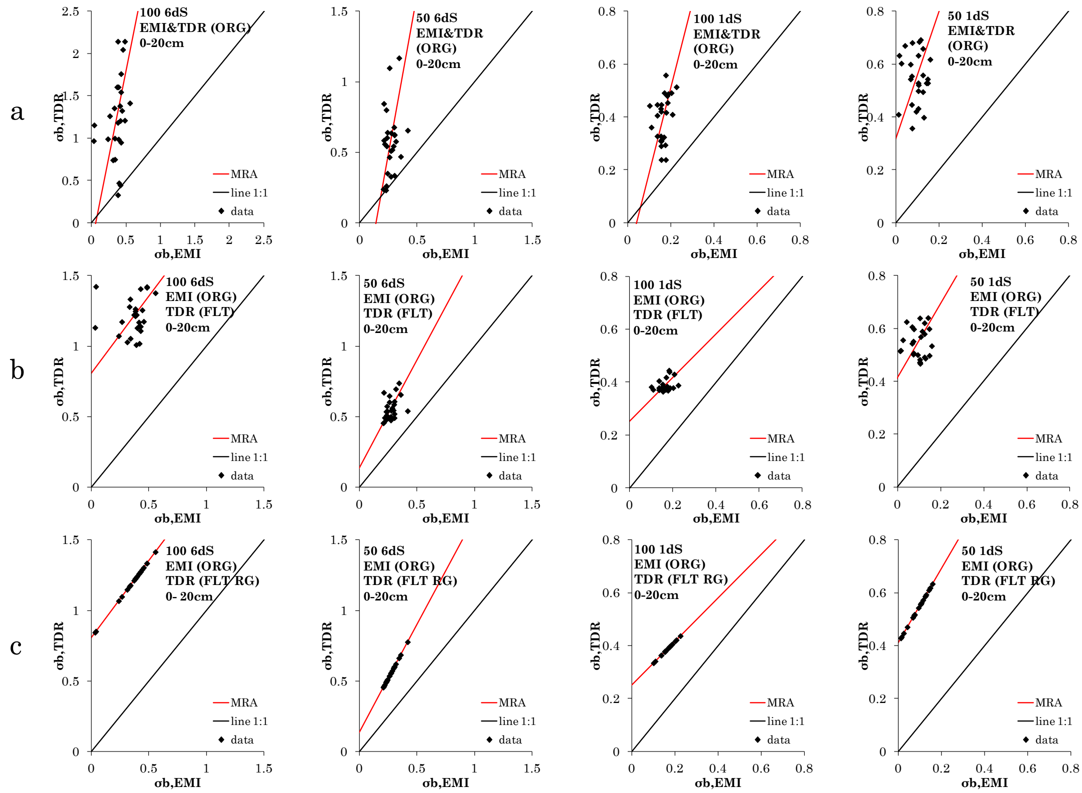

Figure 3. Comparison between $\sigma_{b,TDR}$ and $\sigma_{b,EMI}$ for all four transects for the depth layer 0-20 cm. The graphs in the horizontal panels are respectively for: (a) Original EMI and TDR data; (b) original EMI and filtered TDR data (c) original EMI and filtered TDR data after regression (RG) based on MRA parameters

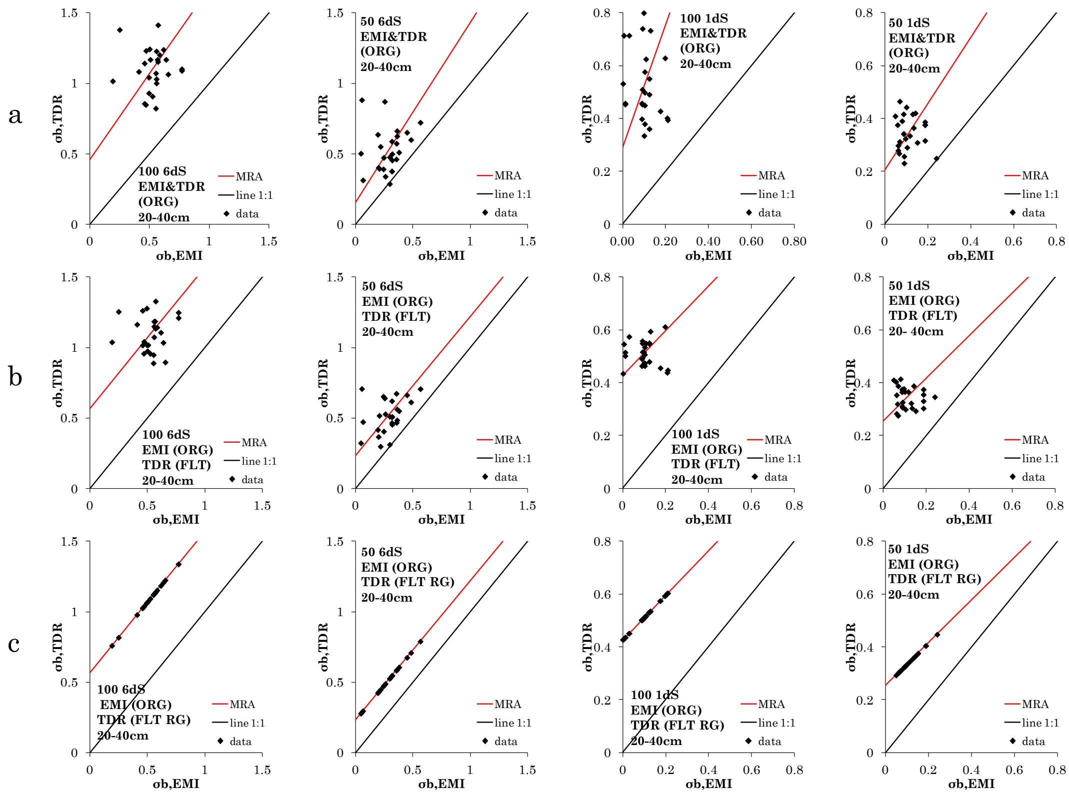

Figure 4. Comparison between $\sigma_{b,TDR}$ and $\sigma_{b,EMI}$ for all four transects for the depth layer 20-40 cm. The graphs in the horizontal panels are respectively for: (a) Original EMI and TDR data; (b) original EMI and filtered TDR data (c) original EMI and filtered TDR data after regression (RG) based on MRA parameters

Hydrol. Earth Syst. Sci. Discuss., doi:10.5194/hess-2017-288, 2017
Manuscript under review for journal Hydrol. Earth Syst. Sci.
Discussion started: 30 May 2017

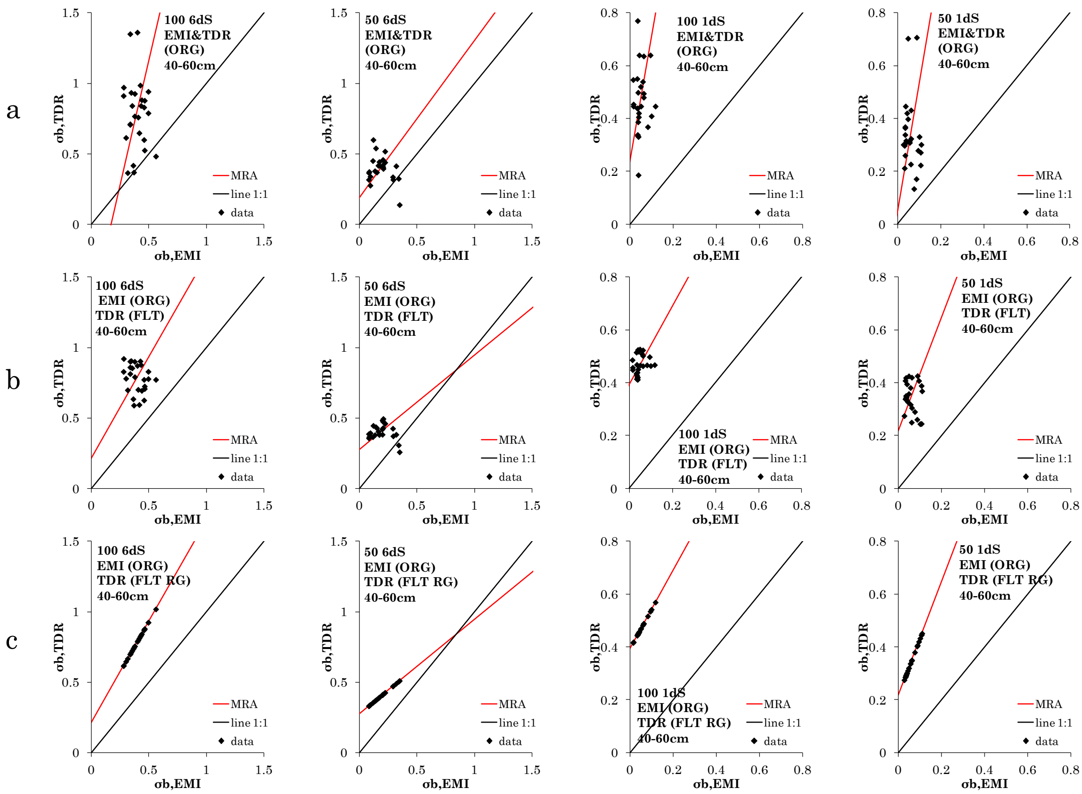

Figure 5. Comparison between $\sigma_{b,TDR}$ and $\sigma_{b,EMI}$ for all four transects for the depth layer 40-60 cm. The graphs in the horizontal panels are respectively for: (a) Original EMI and TDR data; (b) original EMI and filtered TDR data (c) original EMI and filtered TDR data after regression (RG) based on MRA parameters

Hydrol. Earth Syst. Sci. Discuss., doi:10.5194/hess-2017-288, 2017
Manuscript under review for journal Hydrol. Earth Syst. Sci.
Discussion started: 30 May 2017

Hydrology and Earth System Sciences
Open Access
Discussions

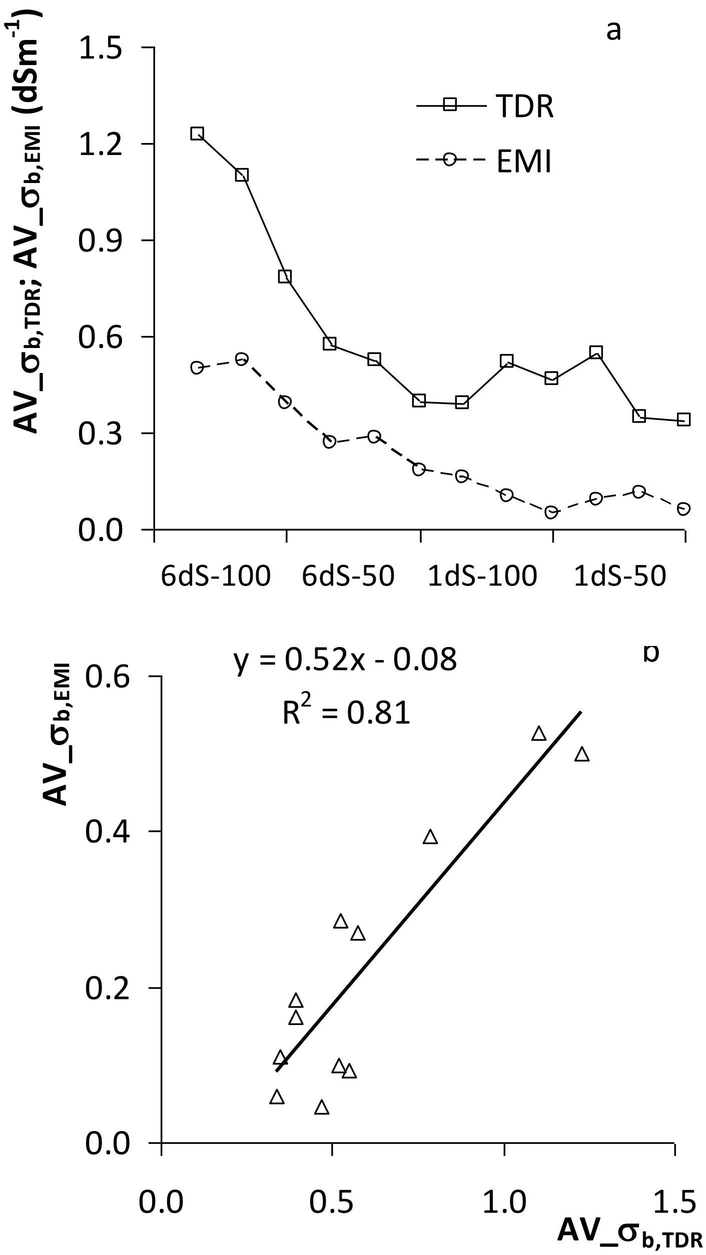

Figure 6. (a) Comparison of the means for the two original series (open squares-solid line for TDR, open circles-dashed line for EMI); (b) The same comparison on a 1:1 plot (open triangles-solid regression line). In figure 6a the four treatments are shown in sequence. For each treatment, the three values are for the three depths (0-20, 20-40 and 40-60 cm)

Hydrol. Earth Syst. Sci. Discuss., doi:10.5194/hess-2017-288, 2017
Manuscript under review for journal Hydrol. Earth Syst. Sci.
Discussion started: 30 May 2017

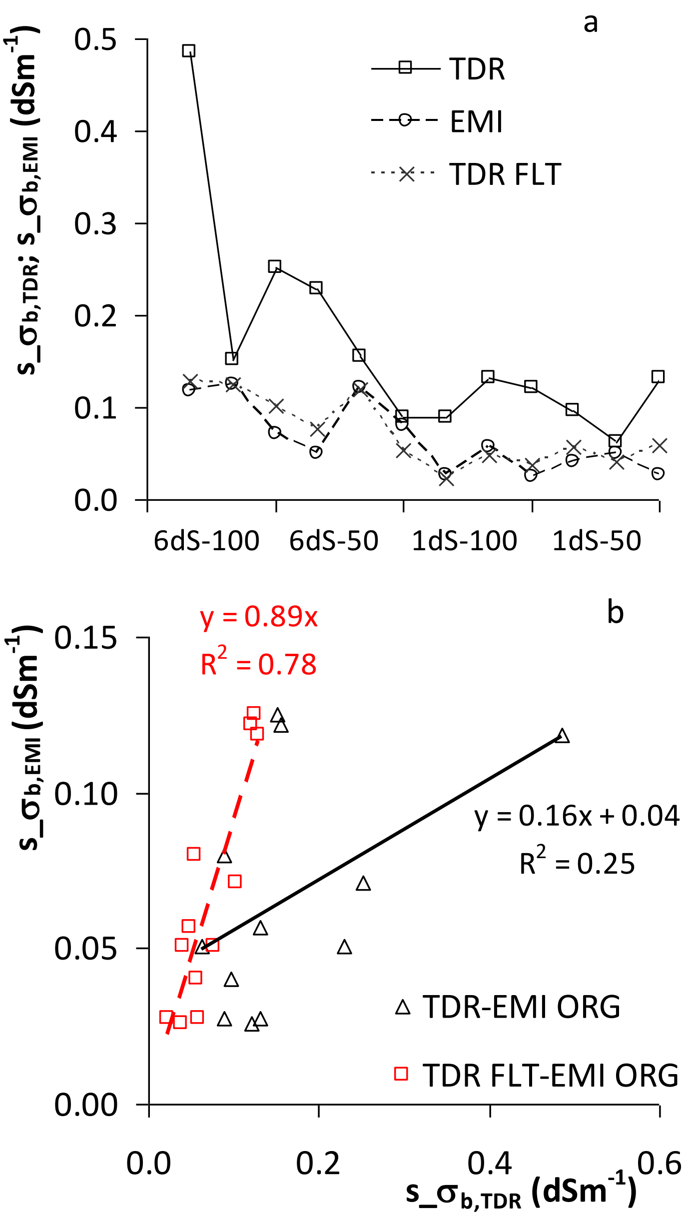

Figure 7. (a) Comparison of the standard deviations of the TDR original series (open squares-solid line), of the EMI original series (open circles-dashed line) and of the filtered TDR series (crosses-dashed line); (b) The same comparison on a 1:1 plot: original TDR and EMI data (open triangles-solid regression line); filtered TDR and original EMI data (open squares-dashed regression line). In figure 7a the four treatments are shown in sequence. For each treatment, the three values are for the three depths (0-20, 20-40 and 40-60 cm)

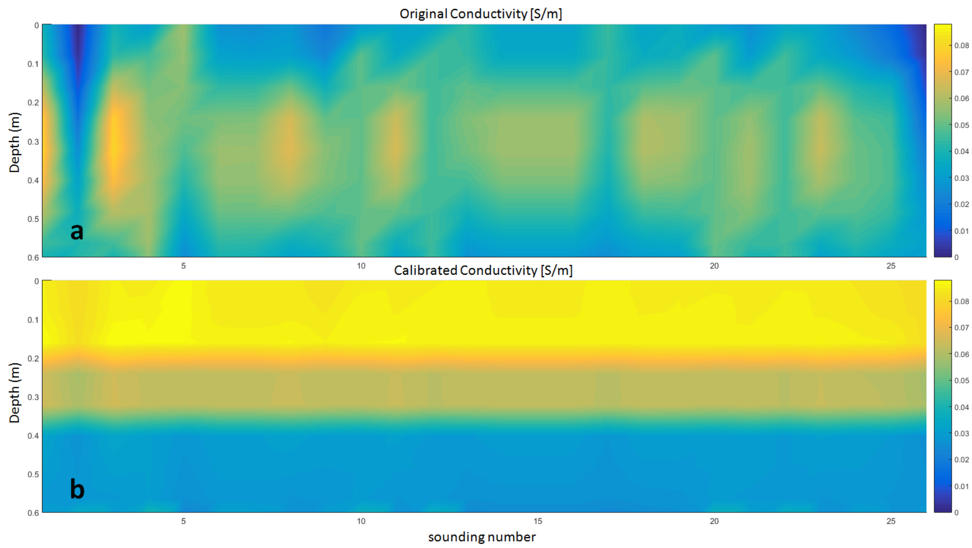

Figure 8. Maps of bulk electrical conductivity for the 100-6dS transect obtained respectively by plotting the original $\sigma_{b,EMI}$ (a) coming from the inversion of the EMI signal and the calibrated $\sigma^{rg}_{b,TDR(FLT)}$ (b) obtained by applying the equation 18 to the $\sigma_{b,EMI}$ data of the first map

Table 1. Concordance parameters for the four transects at depth 0-20 cm. The table reports the Concordance, ρ_L, and the Pearson, ρ_P, correlation, as well as parameters α and β of the MRA line. The bias factor, C_b, is also shown.

Graph panel	C_b 20cm	ρ_L 20cm	ρ_P 20cm	β 20cm	α 20cm
1dS-100					
a	0.08	0.02	0.31	3.20	-0.13
b	0.02	0.01	0.35	0.82	0.25
c	0.02	0.02	0.96	0.82	0.25
1dS-50					
a	0.04	0.0002	-0.01	2.39	0.32
b	0.02	0.0006	0.03	1.40	0.41
c	0.02	0.02	0.96	1.4	0.41
6dS-100					
a	0.12	0.03	0.25	4.10	-0.27
b	0.04	0.005	0.12	1.09	0.81
c	0.04	0.04	0.96	1.09	0.81
6dS-50					
a	0.16	0.03	0.22	4.52	-0.65
b	0.09	0.04	0.42	1.52	0.14
c	0.09	0.08	0.96	1.52	0.14

Table 2. Concordance parameters for the four transects at depth 20-40 cm. The table reports the Concordance, **ρ_L**, and the Pearson, **ρ_P**, correlation, as well as parameters α and β of the MRA line. The bias factor, C_b, is also shown.

Graph panel	C_b 40cm	ρ_L 40cm	ρ_P 40cm	β 40cm	α 40cm
			1dS-100		
a	0.08	-0.02	-0.21	2.32	0.29
b	0.03	-0.002	-0.07	0.84	0.43
c	0.03	0.03	0.96	0.84	0.43
			1dS-50		
a	0.10	-0.004	-0.04	1.25	0.21
b	0.07	-0.01	-0.13	0.81	0.25
c	0.07	0.07	0.96	0.81	0.25
			6dS-100		
a	0.10	0.001	0.01	1.21	0.46
b	0.09	0.004	0.05	0.99	0.57
c	0.09	0.08	0.96	0.99	0.57
			6dS-50		
a	0.40	0.06	0.15	1.27	0.16
b	0.35	0.14	0.39	0.98	0.24
c	0.35	0.34	0.96	0.98	0.24

Hydrology and Earth System Sciences
Open Access
Discussions

Table 3. Concordance parameters for the four transects at depth 40-60cm. The table reports the Concordance, **ρ_L**, and the Pearson, **ρ_P**, correlation, as well as parameters α and β of the MRA line. The bias factor, C_b, is also shown.

Graph panel	C_b 60cm	ρ_L 60cm	ρ_P 60cm	β 60cm	α 60cm
1dS-100					
a	0.03	0.002	0.07	4.69	0.25
b	0.01	0.003	0.24	1.48	0.40
c	0.01	0.01	0.96	1.48	0.40
1dS-50					
a	0.08	-0.01	-0.12	4.81	0.05
b	0.04	-0.01	-0.17	2.14	0.22
c	0.04	0.04	0.96	2.14	0.22
6dS-100					
a	0.16	-0.01	-0.09	3.52	-0.60
b	0.09	-0.02	-0.25	1.43	0.22
c	0.09	0.08	0.96	1.43	0.22
6dS-50					
a	0.24	-0.07	-0.27	1.11	0.19
b	0.15	-0.03	-0.18	0.67	0.28
c	0.15	0.15	0.96	0.67	0.28